Díaz-De Armas, A. y Martínez-Ratón, Y. (2017). Role of length polydispersity in the phase behavior of freely rotating hard-rectangle fluids. *Physical Review E*, 95(5), 052702.

DOI: https://doi.org/10.1103/PhysRevE.95.052702

Role of length polydispersity in the phase behavior of freely rotating hard-rectangle fluids

Ariel Díaz-De Armas* and Yuri Martínez-Ratón†
Grupo Interdisciplinar de Sistemas Complejos, Departamento de Matemáticas, Escuela Politécnica Superior, Universidad Carlos III de Madrid, Avenida de la Universidad 30, 28911 Leganés, Madrid, Spain
(Received 7 February 2017; published 22 May 2017)

We use the density-functional formalism, in particular the scaled-particle theory, applied to a length-polydisperse hard-rectangle fluid to study its phase behavior as a function of the mean particle aspect ratio κ_0 and polydispersity Δ_0. The numerical solutions of the coexistence equations are calculated by transforming the original problem with infinite degrees of freedoms to a finite set of equations for the amplitudes of the Fourier expansion of the moments of the density profiles. We divide the study into two parts. The first one is devoted to the calculation of the phase diagrams in the packing fraction η_0-κ_0 plane for a fixed Δ_0 and selecting parent distribution functions with exponential (the Schulz distribution) or Gaussian decays. In the second part we study the phase behavior in the η_0-Δ_0 plane for fixed κ_0 while Δ_0 is changed. We characterize in detail the orientational ordering of particles and the fractionation of different species between the coexisting phases. Also we study the character (second vs first order) of the isotropic-nematic phase transition as a function of polydispersity. We particularly focus on the stability of the tetratic phase as a function of κ_0 and Δ_0. The isotropic-nematic transition becomes strongly of first order when polydispersity is increased: The coexistence gap widens and the location of the tricritical point moves to higher values of κ_0 while the tetratic phase is slightly destabilized with respect to the nematic one. The results obtained here can be tested in experiments on shaken monolayers of granular rods.

DOI: 10.1103/PhysRevE.95.052702

I. INTRODUCTION

Size polydispersity is an important feature present in experiments conducted on colloidal suspensions of anisotropic, rod or platelike, particles [1–10]. The process of synthesis of mineral particles cannot avoid the presence of polydispersity in sizes and only a sequence of fractionation steps can reduce it considerably. In experimental situations the number of species with different sizes is so large that we can consider a continuous size polydispersity as a reasonable approximation. However, the inclusion of a continuous size polydispersity in theoretical models considerably complicates their numerical implementation. This constitutes the reason why the method of moments was developed as a powerful theoretical tool to approximately solve the equations resulting from the two-phase coexistence calculations [11–14]. The polydispersity is present not only in colloids but also in biological [15] and granular [16] systems. The polymerization of F-actin filaments confined to quasi-two-dimensional geometries constitutes a particular realization of a two-dimensional liquid-crystal system made of polydisperse flexible rods [17].

Several experimental [1–10] and theoretical [18–32] works have studied the effect of polydispersity in particle sizes on the phase behavior and orientational ordering properties of colloidal suspensions made of anisotropic particles. Some general trends found in these studies concerning to the isotropic-nematic (I-N) phase transition can be summarized as follows. (i) The polydispersity dramatically widens the region of I-N two-phase coexistence, i.e., the density gap between the cloud and shadow points is considerably enlarged, making this transition strongly of first order. (ii) There exists strong fractionation in sizes between coexisting phases from which small and large particles usually populate the I and N phases, respectively. The above-mentioned experimental and theoretical works were conducted on three-dimensional systems, however the effect of polydispersity on two-dimensional (2D) liquid-crystals has been scarcely explored [33–37]. An experimental realization of a quasi-2D liquid-crystal system, apart from that already pointed out before, can be obtained by vertically shaking a monolayer of granular rods. Recent experiments on these monolayers showed the presence of liquid-crystal textures as stationary states [38–41].

Theoretical studies on 2D monodisperse hard rods have shown that the transition from the high-density N phase (without long-range orientational order) to the low-density I phase is continuous, via a Kosterlitz-Thouless disclination unbinding type of mechanism [42], rather than first order [43,44]. However, recent studies proved that when particle interactions are of a certain type the I-N transition becomes of first order in two dimensions [45,46]. A recent controversy resulted on the universality class (Ising vs that corresponding to $q = 1$ Potts-type models) of the I-N transition of hard Zwanzig self-assembled rods on a lattice [35,36]: A mean-field theory shows that these polydisperse self-assembled rods exhibit a first-order I-N transition while Monte Carlo results discard this fact [47]. Finally, a recent experiment on two-dimensional polydisperse hard rods (where magnetic nanorods were strongly confined between layers of a lamellar phase) has shown a first-order I-N transition [37].

The particular shape of two-dimensional rods is also determinant to stabilize the N or tetratic (T) phases at low aspect ratios κ. In the latter the angular distribution function is invariant under $\pi/2$ rotations. Hard ellipses (HEs) [48–51] and hard discorectangles (HDRs) [43] only show the usual I-N transition followed by transitions to the plastic or orientationally ordered crystals. Hard rectangles (HRs), on the other hand, also show fluid or crystalline phases with tetratic symmetry at low κ_0 [52–57]. The T phase of HR was theoretically predicted

*ardiaza@math.uc3m.es
†yuri@math.uc3m.es

by mean-field density-functional (DF) studies [52,54]. Monte Carlo simulations on hard squares showed the presence of strong tetratic correlations of quasi-long-range order [53] and simulations on HRs of $\kappa_0 = 2$ showed a liquid with the same T correlations and no N order [55]. The solid phase in the latter system was observed with a nonperiodic T ordering and having the structure of a random tiling of the square lattice with dimers of HRs randomly oriented [55]. Experiments on a monolayer of disks standing on edges observed the conventional Kosterlitz-Thouless transition from I to N with almost smectic behavior at high density. However, on the isotropic side of the I-N transition an unusual regime of short-range T correlations dominates over N ones [58]. Recent experiments on monolayers of hard microscale square platelets showed a phase transition between a hexagonal rotator crystal and a rhombic crystal as the packing fraction is increased [59]. The absence of T ordering in this system was further explained by resorting to the roundness of the square corners [60]. If the roundness is sufficiently small the particles behave like perfect squares and the T phase is recovered [60]. Shaken monolayers of granular cubes [61] and cylinders [38,41,62] exhibit stationary textures with strong T ordering even for aspect ratios of cylinders as large as 7.

All these studies show the profound effect that particle shapes and pair interactions have on the symmetry of the orientationally ordered phases. Even the character (continuous vs first order) can be influenced by them. The mean-field scaled-particle theory (SPT) for HRs predicts a first-order I-N (or T-N) transition located between two tricritical points. This is a peculiar feature of HRs because the I-N transition for HDRs and HEs following the same theory is always of second order [54]. This difference can be explained by the peculiar form of the excluded volume between two HRs, as it will be discussed in Sec. II B.

The main purpose of the present work is to study how the polydispersity affects the phase behavior of HRs. To this purpose we will extend the mean-field SPT formalism from its multicomponent version (already described in Refs. [63,64]) to the length-polydisperse case. The minor length of rectangles is considered constant while the major one is polydisperse according to a Schulz-type (with exponential decay) probability density distribution and also according to a distribution with a Gaussian decay. We calculated the phase diagrams for a fixed Δ_0 while κ_0 varies and also for certain fixed values of κ_0 while Δ_0 changes. We measured the degrees of orientational ordering of particles and their fractionation between the coexisting phases. The addition of polydispersity dramatically increases the interval of aspect ratios where the I-N is of first order and the I-N tricritical point moves to higher values of κ_0. Also we prove that the stability of the T phase is not severely affected by polydispersity: The area of the phase diagram where the T phase is stable does not decrease substantially when the polydispersity is increased from zero to its maximum allowed value.

II. MODEL AND THEORY

In this section we present the theoretical tools used to study the phase behavior of a length-polydisperse HR fluid. In Sec. II A we formulate the HR model and define the family of length-polydisperse probability distributions we have used. In Sec. II B we generalize the SPT formalism from the multicomponent HR mixture [63] to a continuous polydisperse fluid. Further, we explicitly obtain the set of equations used in Sec. II C to calculate the two-phase coexistence, giving also details on their numerical implementation. A concise summary of the I-N, I-T, and T-N bifurcation analysis will be given in Sec. II D. Finally, in Sec. II E we define the main variables and functions used to measure the orientational ordering and fractionation between coexisting phases.

A. Polydisperse HR model

Our model consists of a collection of freely rotating HRs. They move and rotate in two dimensions and cannot overlap. We take the minor edge length of rectangles σ to be constant, while its mayor length L (with $\sigma < L < \infty$), defining the main particle axis, is considered continuously polydisperse according to a fixed, so-called parent, probability density distribution function

$$f_0(\kappa) = C_{\nu,q}(\kappa_0)\left(\frac{\kappa-1}{\kappa_0-1}\right)^{\nu} \exp\left[-\lambda_{\nu,q}\left(\frac{\kappa-1}{\kappa_0-1}\right)^{q}\right], \quad (1)$$

$$C_{\nu,q}(\kappa_0) = q(\kappa_0-1)^{-1}\frac{\Gamma^{\nu+1}[(\nu+2)/q]}{\Gamma^{\nu+2}[(\nu+1)/q]}, \quad (2)$$

$$\lambda_{\nu,q}^{1/q} = \frac{\Gamma[(\nu+2)/q]}{\Gamma[(\nu+1)/q]}, \quad (3)$$

defined in terms of the particle aspect ratio $\kappa \equiv L/\sigma$. This function is normalized to unity $\int_1^\infty d\kappa f_0(\kappa) = 1$ and its first moment $\langle\kappa\rangle \equiv \int_1^\infty d\kappa\, \kappa\, f_0(\kappa) = \kappa_0$ is selected to be equal to κ_0 (the mean aspect ratio). The polydisperse coefficient, or mean-square deviation, can be calculated as

$$\Delta \equiv \sqrt{\frac{\langle\kappa^2\rangle - \langle\kappa\rangle^2}{\langle\kappa\rangle^2}} = \left(1-\frac{1}{\kappa_0}\right)\Delta_0, \quad (4)$$

$$\Delta_0 \equiv \sqrt{\frac{\Gamma[(\nu+1)/q]\Gamma[(\nu+3)/q]}{\Gamma^2[(\nu+2)/q]} - 1}, \quad (5)$$

where $\Gamma(x)$ is the standard Gamma function. The parameters ν and q, used to define the family of functions (1), control the width of $f_0(\kappa)$, with q being the one that dictates the decay of the tail: For $q = 1$ (corresponding to the Schulz distribution function) we obtain an exponential decay, while for $q = 2$ a Gaussian tail is obtained. In the following we will use Δ_0 as a measure of the degree of length polydispersity. To exemplify the shapes of the distributions following Eq. (1) we plot them in Fig. 1 for $\kappa_0 = 3$, polydispersity values $\Delta_0 = 0.408$ (black lines) and $\Delta_0 = 0.250$ (gray lines), and decay parameters $q = 1$ (solid lines) and $q = 2$ (dashed lines).

B. The SPT for length-polydisperse HRs

We use the SPT formalism for a multicomponent HR fluid [63] extended to the continuously length-polydisperse limit $\rho_\nu(\phi) \to \rho(\kappa,\phi)$, where $\rho_\nu(\phi)$ corresponds to the angular density profile of species ν of the multicomponent mixture, while $\rho(\kappa,\phi)$ denotes the continuously distributed angular density profile of species with aspect ratio κ. All sums over species in equations used to define the free-energy density in

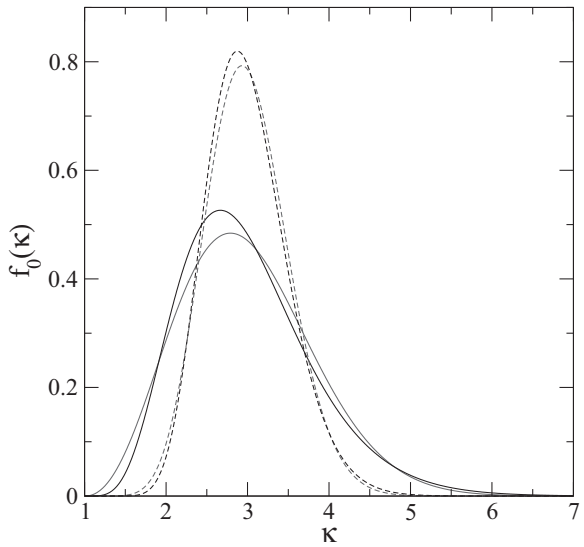

FIG. 1. Distribution functions from Eq. (1) for $\kappa_0 = 3$ and $\Delta_0 = 0.408$ (black lines) and $\kappa_0 = 3$ and $\Delta_0 = 0.250$ (gray lines), with $q = 1$ (solid lines) and $q = 2$ (dashed lines).

Ref. [63] are now substituted by integrals over the aspect ratio $\sum_\nu \to \int d\kappa$. The resulting free-energy density in reduced thermal units $\Phi[\rho] \equiv \Phi_{\rm id}[\rho] + \Phi_{\rm ex}[\rho]$, split into its ideal and excess contributions $\Phi_{\rm id}[\rho]$ and $\Phi_{\rm ex}[\rho]$, respectively, is a functional of $\rho(\kappa,\phi)$:

$$\Phi_{\rm id}[\rho] \equiv \beta\mathcal{F}_{\rm id}[\rho]/A = \int d\kappa \int d\phi\, \rho(\kappa,\phi)[\ln \rho(\kappa,\phi) - 1], \tag{6}$$

$$\Phi_{\rm ex}[\rho] \equiv \beta\mathcal{F}_{\rm id}[\rho]/A = -\rho_0^{(0)} \ln\left(1 - \rho_0^{(1)}\sigma^2\right) + \frac{S_0[\rho]}{1 - \rho_0^{(1)}\sigma^2}, \tag{7}$$

$$S_0[\rho] \equiv \int d\kappa_1 \int d\kappa_2 \int d\phi_1 \int d\phi_2 \rho(\kappa_1,\phi_1)\rho(\kappa_2,\phi_2) \times A_0(\kappa_1,\kappa_2,\phi_1 - \phi_2), \tag{8}$$

$$A_0(\kappa_1,\kappa_2,\phi) = \frac{\sigma^2}{2}\{(\kappa_1\kappa_2 + 1)|\sin\phi| + (\kappa_1 + \kappa_2)|\cos\phi|\}. \tag{9}$$

In Eqs. (6) and (7), $\beta \equiv 1/k_BT$ is the Boltzmann factor, $\mathcal{F}_{\rm id,ex}[\rho]$ denotes the ideal and excess parts of the free-energy density functional, and A is the total area of the system. We have also defined the ith moment of the integrated, over κ and ϕ, density profile

$$\rho_0^{(i)} \equiv \int_0^\pi d\phi\, \rho^{(i)}(\phi) = \int_0^\pi d\phi \left[\int_1^\infty d\kappa\, \kappa^i \rho(\kappa,\phi)\right], \tag{10}$$

where $i = 1,2$ and the integration with respect to ϕ was taken between 0 and π (instead of 2π) due to the head-tail symmetry of rectangles. Note that these moments can be obtained from the ith moment angular profile $\rho^{(i)}(\phi)$ as defined in Eq. (10). The magnitude $A_0(\kappa_1,\kappa_2,\phi)$ is directly related to the excluded area $A_{\rm excl}(\kappa_1,\kappa_2,\phi)$ between two HRs of aspect ratios κ_1 and κ_2 with a relative angle between their main axes equal to ϕ. The relation between both magnitudes is $2A_0(\kappa_1,\kappa_2,\phi) = A_{\rm excl}(\kappa_1,\kappa_2,\phi) - (\kappa_1 + \kappa_2)\sigma^2$. In Fig. 2(a) we schematically show the excluded volume between two HRs of $\kappa = 2$, while in Fig. 2(b) we show the function $A_{\rm excl}(2,2,\phi)$. The secondary minimum at $\phi = \pi/2$ is responsible for the stability of the T phase at low aspect ratios, which is a peculiar property almost unique to the rectangular shape. The most common functional form of the excluded area is exemplified for HDRs in Fig. 2(b) for comparison (note the presence of a maximum at $\pi/2$ instead of a local minimum).

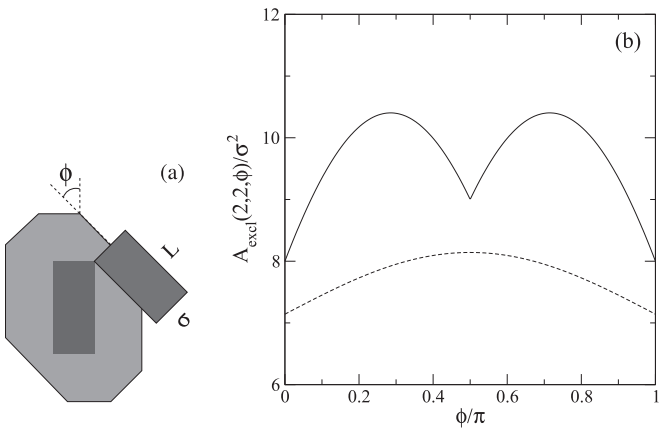

FIG. 2. (a) Sketch of the excluded area between two HRs of aspect ratio $\kappa = L/\sigma = 2$ and relative angle ϕ between their long axes. (b) Excluded areas in units of σ^2 between two HRs (solid lines) and two HDRs (dashed lines) of the same aspect ratio $\kappa = 2$.

C. Coexistence calculations and numerical schemes

We now proceed to present the set of equations we used to calculate the phase coexistence between two phases with different orientational symmetries (I, N, or T phases). The total free-energy density of a phase-separated system with a fraction γ_α of the total volume occupied by phase α ($\alpha = I,N,T$) can be expressed as $\Phi^{(t)}[\rho] = \sum_\alpha \gamma_\alpha \Phi^{(\alpha)}[\rho]$ (obviously $\sum_\alpha \gamma_\alpha = 1$).

From now on the coexistence between (I,T) and N phases occupying fractions of the total volume $\gamma_{I,T} = \gamma_0$ and $\gamma_N = 1 - \gamma_0$, respectively, will be denoted by $(I,T)_{\gamma_0}$-$N_{1-\gamma_0}$. For example, I_0-N_1 coexistence implies that the I phase occupies a vanishing small volume (the so-called shadow phase), while the N phase takes up the total volume (the so-called cloud phase).

The lever rule guarantees the conservation of the total number of species of aspect ratio κ:

$$\rho_0 f_0(\kappa) = \frac{1}{\pi}\sum_\alpha \gamma_\alpha \int_0^\pi d\phi\, \rho^{(\alpha)}(\kappa,\phi), \tag{11}$$

where $\rho_0 = N/A$ (with N the total number of particles) is the total number density of the system. Using (11) as a constraint in the minimization of the total free-energy density $\Phi^{(t)}[\rho]$ with respect to $\rho^{(\alpha)}(\kappa,\phi)$ gives us the following set of equations:

$$\rho^{(\alpha)}(\kappa,\phi) = \frac{\rho_0 f_0(\kappa) \exp\left[-\beta\mu_{\rm ex}^{(\alpha)}(\kappa,\phi)\right]}{\pi^{-1}\sum_\tau \gamma_\tau \int_0^\pi d\phi' \exp\left[-\beta\mu_{\rm ex}^{(\tau)}(\kappa,\phi')\right]}, \tag{12}$$

where $\alpha \in \{I,T,N\}$ and the excess chemical potential of the coexisting α phase is defined as $\beta\mu_{\rm ex}^{(\alpha)}(\kappa,\phi) = \frac{\delta\Phi_{\rm ex}^{(\alpha)}[\rho]}{\delta\rho^{(\alpha)}(\kappa,\phi)}$. From now on we will use greek letters $\alpha,\tau,\ldots$ as superscripts to label coexisting phases, while the latin letters $i,j,\ldots$ will be used to label the moments.

The numerical procedure used to solve Eq. (12) is based on the reduction of this infinite set of equations (note that κ and ϕ are continuous variables) to a finite set. To this purpose we first introduce a truncated Fourier expansion of the moment profiles

$$\rho^{(i,\alpha)}(\phi) = \frac{1}{\pi}\sum_{j=0}^{N}\rho_j^{(i,\alpha)}\cos(2j\phi), \tag{13}$$

with $\{\rho_j^{(i,\alpha)}\}$ the Fourier amplitudes. Second we substitute this expansion into $\beta\mu_{\rm ex}^{(\alpha)}(\kappa,\phi)$, multiply (12) by $\kappa^i\cos(2j\phi)$, and integrate over κ and ϕ to obtain a closed set of equations

$$\rho_j^{(i,\alpha)} = \rho_0 D_{j0}\int_1^\infty d\kappa\,\kappa^i f_0(\kappa)\frac{T_j^{(\alpha)}(\kappa)}{\sum_\tau \gamma_\tau T_0^{(\tau)}(\kappa)}, \tag{14}$$

$$T_j^{(\tau)}(\kappa) \equiv \pi^{-1}\int_0^\pi d\phi\,\exp\left[-\beta\mu_{\rm ex}^{(\tau)}(\kappa,\phi)\right]\cos(2j\phi), \tag{15}$$

where $j = 1,\ldots,N$; $i = 0,1$; and $D_{j0} = 2/(1+\delta_{j0})$ with δ_{j0} the Kronecker delta. The success of the present strategy is based on the dependence of the excess part of the chemical potential on the angular density profile $\rho(\kappa,\phi)$ only through its moments $\{\rho_j^{(i,\alpha)}\}$:

$$\beta\mu_{\rm ex}^{(\alpha)}(\kappa,\phi) = -\ln\left[1-\rho_0^{(1,\alpha)}\sigma^2\right] + \frac{S_1^{(\alpha)}(\kappa,\phi)}{1-\rho_0^{(1,\alpha)}\sigma^2} + \beta p^{(\alpha)}\kappa\sigma^2, \tag{16}$$

$$S_1^{(\alpha)}(\kappa,\phi) \equiv \frac{2\sigma^2}{\pi}\left\{\left(\rho_0^{(1,\alpha)}+\rho_0^{(0,\alpha)}\right)(\kappa+1) - \sum_{j\geqslant 1}\frac{\left[\rho_j^{(1,\alpha)}+(-1)^j\rho_j^{(0,\alpha)}\right][\kappa+(-1)^j]}{4j^2-1}\cos(2j\phi)\right\}, \tag{17}$$

$$\beta p^{(\alpha)} = \frac{\rho_0^{(0,\alpha)}}{1-\rho_0^{(1,\alpha)}\sigma^2} + \frac{S_0^{(\alpha)}[\rho]}{\left[1-\rho_0^{(1,\alpha)}\sigma^2\right]^2}, \tag{18}$$

$$S_0^{(\alpha)}[\rho] = \frac{\sigma^2}{\pi}\left[\left(\rho_0^{(1,\alpha)}+\rho_0^{(0,\alpha)}\right)^2 - \frac{1}{2}\sum_{j\geqslant 1}\frac{\left(\rho_j^{(1,\alpha)}+(-1)^j\rho_j^{(0,\alpha)}\right)^2}{4j^2-1}\right], \tag{19}$$

where $\beta p^{(\alpha)}$, defined in Eq. (18), is the pressure of phase α. Thus we finally obtain a closed set of equations (14) to be solved for the Fourier amplitudes $\{\rho_j^{(i,\alpha)}\}$. This set in turn guarantees the equality between chemical potentials of each species in both coexisting phases. An equation corresponding to the equality between pressures at each phase should be added to get the mechanical equilibrium and consequently the pressure in Eq. (16) can be dropped during the numerical implementation of (14). We have selected a total number N of Fourier coefficients in Eq. (13) in such a way as to guarantee that $|\rho_N^{(i,\alpha)}| < 10^{-4}$. In most cases $N \lesssim 20$ is enough to reach this criterion even when the transition to the orientationally ordered phases is strongly of first order. A fixed point iteration method was used to solve (14). To perform the numerical integrals over ϕ and κ in Eqs. (14) and (15) we used, after some convenient changes of variables, Gauss-Legendre and Gauss-Laguerre quadratures, respectively. Once the numerical convergence of Eq. (14) was reached for a fixed ρ_0, we used the equality

$$p^{(\alpha)}\left(\left\{\rho_j^{(i,\alpha)}\right\},\rho_0\right) = p^{(\beta)}\left(\left\{\rho_j^{(i,\beta)}\right\},\rho_0\right), \tag{20}$$

numerically solved using Brent's root-finding method, to find the value of ρ_0 at equilibrium.

D. Bifurcation analysis

To find the onset of N and T ordering from the I phase we performed a bifurcation analysis of Eq. (14) for the case of $\gamma_I = 1$, with respect to the small Fourier amplitudes $\{\rho_j^{(i,\alpha)}\}$ ($j = 1$ for $\alpha = N$ while $j = 2$ for $\alpha = T$). The resulting packing fractions $\eta_0 \equiv \rho_0\kappa_0\sigma^2$ at which the I phase is destabilized with respect to the N and T phases, the so-called spinodal instability in the case of a first-order first transition or the second-order line (SOL) in the case of a continuous phase transition, have the following analytical expressions:

$$\eta_0^{(I\text{-}N)} = \left\{1+\frac{2}{3\pi\kappa_0}(\kappa_0-1)^2\left(1+\Delta_0^2\right)\right\}^{-1}, \tag{21}$$

$$\eta_0^{(I\text{-}T)} = \left\{1+\frac{2}{15\pi\kappa_0}\left[(\kappa_0+1)^2+(\kappa_0-1)^2\Delta_0^2\right]\right\}^{-1}. \tag{22}$$

For small (large) mean aspect ratios κ_0 it is expected that the I phase destabilizes first with respect to the T (N) phase. Consequently, there should exist a crossing point κ_0^* between both I-T and I-N spinodals. This point can be calculated from the equality $\eta_0^{(I\text{-}N)} = \eta_0^{(I\text{-}T)}$, which results in

$$\kappa_0^* = \frac{3+2\Delta_0^2+\sqrt{5+4\Delta_0^2}}{2\left(1+\Delta_0^2\right)}. \tag{23}$$

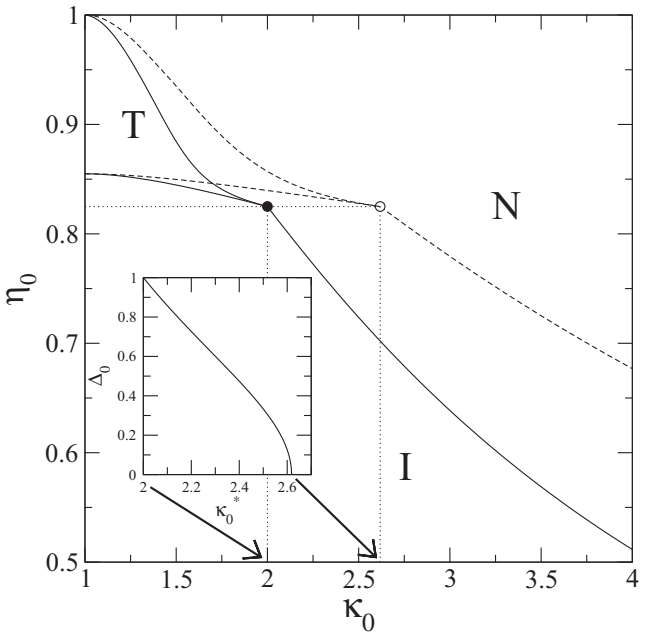

FIG. 3. Plot of the I-N, I-T, and T-N bifurcation curves: packing fraction vs mean aspect ratio κ_0 for $\Delta_0 = 0$ (dashed lines) and $\Delta_0 = 1$ (solid lines). The inset shows the polydisperse coefficient Δ_0 as a function of the critical value κ_0^* for which $\eta_0^{(I\text{-}N)} = \eta_0^{(I\text{-}T)}$ (the closed and open circles in the main figure). The stability regions of the I, N, and T phases are correspondingly labeled.

From this equation we obtain, for the one-component fluid ($\Delta_0 = 0$), the value $\kappa_0^* = 1 + \varphi$ with $\varphi = (1+\sqrt{5})/2 \approx 1.618$ the golden ratio. For the highest polydispersity $\Delta_0 = 1$ (reached for the Schulz distribution) we obtain $\kappa_0^* = 2$. Thus we can extract as a preliminary conclusion that the stability of the T phase slightly decreases with polydispersity.

For small aspect ratios $\kappa_0 \sim 1$, a stable T phase is expected up to the density at which a T-N transition takes place. To calculate the T-N SOL we have performed a bifurcation analysis of Eq. (14), particularized for $\gamma_T = 1$, with respect to the small Fourier components $\{\rho_1^{(i,N)}\}$. The obtained result for the packing fraction at the N-T bifurcation can be calculated from

$$\eta_0^{(N\text{-}T)} = \left\{1 + \frac{2}{3\pi\kappa_0}\left[(\kappa_0 - 1)^2\left(1 + \Delta_0^2\right) + \chi_2\left(\eta_0^{(N\text{-}T)}\right)\right]\right\}^{-1}, \tag{24}$$

where we have defined

$$\chi_2(\eta_0) = \int d\kappa\, f_0(\kappa)(\kappa - 1)^2 \frac{T_2^{(T)}(\kappa)}{T_0^{(T)}(\kappa)}, \tag{25}$$

with the functions $T_j^{(T)}(\kappa)$, already defined in Eq. (15), calculated once the Fourier amplitudes $\{\rho_{2j}^{(i,T)}\}$ at the equilibrium T phase were found for a given η_0. We have solved iteratively the nonlinear integral equation (24) with respect to $\eta_0^{(N\text{-}T)}$ to find the N-T SOL.

We plot the three found bifurcation curves $\eta_0^{(I\text{-}N)}(\kappa_0)$, $\eta_0^{(I\text{-}T)}(\kappa_0)$, and $\eta_0^{(N\text{-}T)}(\kappa_0)$ in Fig. 3 for $\Delta_0 = 0$ and 1. We can see that the I-N spinodal is severely affected by polydispersity (is significantly below its one-component counterpart). Another conclusion we can extract from the figure is that the stability of the T phase only slightly decreases with polydispersity as we have already pointed out before by comparing the values of the crossing points κ_0^*. This destabilization can be explained by the presence of long rods (those that destroy the T symmetry) with aspect ratios much larger than κ_0. The long rods have a profound effect on the orientational ordering properties of the fluid, usually favoring the N ordering. However, the decrease in the T phase stability is not as strong as expected because the mean-square deviation Δ of the function $f_0(\kappa)$ decreases with the mean aspect ratio κ_0 [see Eq. (4)]: When $\kappa_0 \to 1$ we obtain $\Delta \to 0$ for any Δ_0.

E. Measuring the orientational ordering and fractionation effects

To present the results in Sec. III it is convenient to define, apart from the above-introduced packing fraction η_0, the following dimensionless variables:

$$\eta_j^{(0,\alpha)} = \rho_j^{(0,\alpha)}\kappa_0\sigma^2, \quad \eta_j^{(1,\alpha)} = \rho_j^{(1,\alpha)}\sigma^2. \tag{26}$$

To measure the orientational ordering of rectangles of aspect ratio κ at the coexisting α phase we use the angular probability distribution function

$$h^{(\alpha)}(\kappa,\phi) \equiv \frac{\rho^{(\alpha)}(\kappa,\phi)}{\int_0^\pi d\phi' \rho^{(\alpha)}(\kappa,\phi')}. \tag{27}$$

The integration of $h^{(\alpha)}(\kappa,\phi)$ over κ gives us the averaged angular distribution function, which, resorting to the Fourier expansion (13), can be easily calculated using the expression

$$\begin{aligned} h^{(\alpha)}(\phi) &\equiv \int d\kappa\, h^{(\alpha)}(\kappa,\phi) \\ &= \left(\pi\rho_0^{(0,\alpha)}\right)^{-1} \sum_j \rho_j^{(0,\alpha)} \cos(2j\phi), \end{aligned} \tag{28}$$

where $\alpha = I, N, T$ labels the distribution of the relevant phase.

The N ($j = 1$) and T ($j = 2$) order parameters are defined through

$$Q_j^{(\alpha)} = \int_0^\pi d\phi\, h^{(\alpha)}(\phi)\cos(2j\phi). \tag{29}$$

Inserting (28) into (29), we obtain

$$Q_j^{(\alpha)} = \frac{\rho_j^{(0,\alpha)}}{2\rho_0^{(0,\alpha)}}. \tag{30}$$

To measure the fractionation between the cloud and shadow coexisting phases we should bear in mind that the cloud phase always has the parent distribution function $f_0(\kappa)$. Thus we will concentrate only on the shadow-phase distribution functions. For the I_1-N_0 and the I_0-N_1 coexistence the distributions corresponding to the N and I shadow phases are

$$f^{(N)}(\kappa) = f_0(\kappa) e^{\beta\mu_{\rm ex}^{(I)}(\kappa)} T_0^{(N)}(\kappa), \tag{31}$$

$$f^{(I)}(\kappa) = f_0(\kappa) \frac{e^{-\beta\mu_{\rm ex}^{(I)}(\kappa)}}{T_0^{(N)}(\kappa)}, \tag{32}$$

while those corresponding to N and T shadow phases of the T_1-N_0 and the T_0-N_1 coexistence are

$$f^{(N)}(\kappa) = f_0(\kappa)\frac{T_0^{(N)}(\kappa)}{T_0^{(T)}(\kappa)}, \tag{33}$$

$$f^{(T)}(\kappa) = f_0(\kappa)\frac{T_0^{(T)}(\kappa)}{T_0^{(N)}(\kappa)}. \tag{34}$$

All these distributions will be normalized as $\tilde{f}^{(\alpha)}(\kappa) \equiv f^{(\alpha)}(\kappa)/\int d\kappa\, f^{(\alpha)}(\kappa)$ for plotting. We will use the averaged over $\tilde{f}^{(\alpha)}(\kappa)$ aspect ratio

$$\langle\kappa\rangle_{\tilde{f}^{(\alpha)}} \equiv \int d\kappa\, \kappa\, \tilde{f}^{(\alpha)}(\kappa) = \frac{\eta_0^{(1,\alpha)}}{\eta_0^{(0,\alpha)}} \tag{35}$$

to quantify the fractionation. Note that it is equal to κ_0 when averaged with respect to $f_0(\kappa)$.

III. RESULTS

In this section we show the results as obtained from the numerical implementation of the SPT DF for length-polydisperse HRs. We divide this section into different subsections, each one devoted to discuss the thermodynamic and orientational properties of polydisperse HRs. In Sec. III A we first describe the resulting phase diagrams using two different parent distribution functions (those with exponential and Gaussian-like decays). Further, we proceed, in Sec. III B, to present a quantitative analysis of the orientational ordering of particles at coexistence. To this purpose we use the angular distribution functions and order parameters. The fractionation of species with different aspect ratios between coexisting phases as a function of the mean aspect ratio and polydispersity is studied in Secs. III C and III D, respectively. Finally, in Sec. III E we study the effect of polydispersity on the location of the I-N tricritical point.

A. Phase diagrams for fixed polydispersity Δ_0

We numerically solved the set of equations (14) together with the mechanical equilibrium condition (20), selecting a parent distribution function (1) with $q = 1$ and a polydisperse coefficient $\Delta_0 = 0.408$, corresponding to the value $\nu = 5$ in Eq. (1). For small mean aspect ratios $\kappa_0 \sim 1$, we calculated the T-N coexistence from Eqs. (14) and (20) fixing the odd Fourier coefficients $\rho_{2j+1}^{(i,T)}$ to zero. This simplification is justified by the symmetry of the T phase: $\rho^{(T)}(\kappa,\phi) = \rho^{(T)}(\kappa,\phi+\pi/2)$. For medium and large aspect ratios we solved the same set of equations, taking into account all the Fourier coefficients $\rho_j^{(i,N)}$ to look for the I-N coexistence. We have found that the I-T transition is always of second order. The total packing fractions η_0 of the I_1 and N_1 (coexisting with their shadow counterparts) phases are shown in Fig. 4. Together with these binodals we also plot the I-N, I-T, and N-T SOLs as calculated in Sec. II D. For comparison we also plot in Fig. 4(a) the phase diagram corresponding to the one-component HR fluid ($\Delta_0 = 0$) calculated in Ref. [54]. The most prominent effects of polydispersity consist of (i) the dramatic broadening of the I-N coexisting region, (ii) the displacement of the I-N tricritical point to higher values of κ_0, and (iii) the lowering of the second-order I-N transition density (the SOL). The widening of the two-phase coexistence region is a well known fact in many studies conducted on three-dimensional polydisperse hard rods [13,14,23,24]. As it is well known, the I-N transition of hard rods in three dimensions is of first order for any aspect ratio. In two dimensions the mean-field

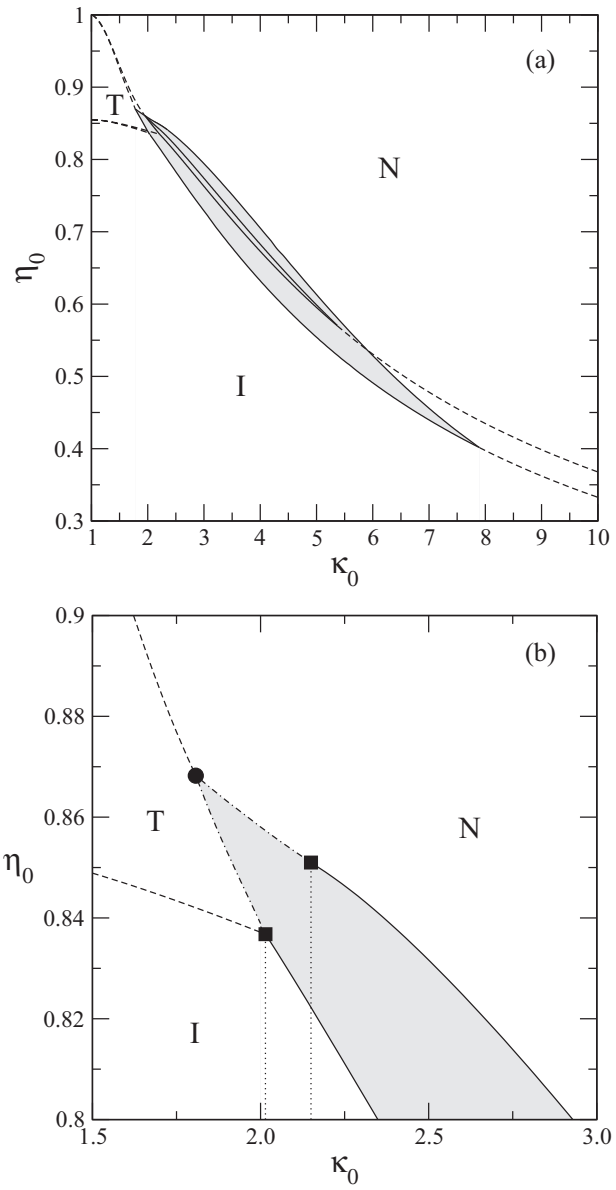

FIG. 4. (a) Phase diagram of the one-component ($\Delta_0 = 0$) and polydisperse ($q = 1$ and $\Delta_0 = 0.408$) HR fluid in the total packing fraction η_0 vs mean aspect ratio κ_0 plane. The one-component fluid exhibits a weaker first-order I-N transition finishing at a tricritical point located well below that of the polydisperse fluid. Shown with solid and dashed lines are the cloud coexistence binodals and SOLs, respectively. Regions of stability of the I, N, and T phases are labeled in the figure. (b) Close-up of the phase diagram of the polydisperse HR shown in (a) around the left tricritical point (closed circle). Shown with dot-dashed lines are the T_1-N_0 and T_0-N_1 cloud coexistence binodals, both ending at the closed squares. Between the vertical dotted lines a possible triple I-N-T coexistence could exist.

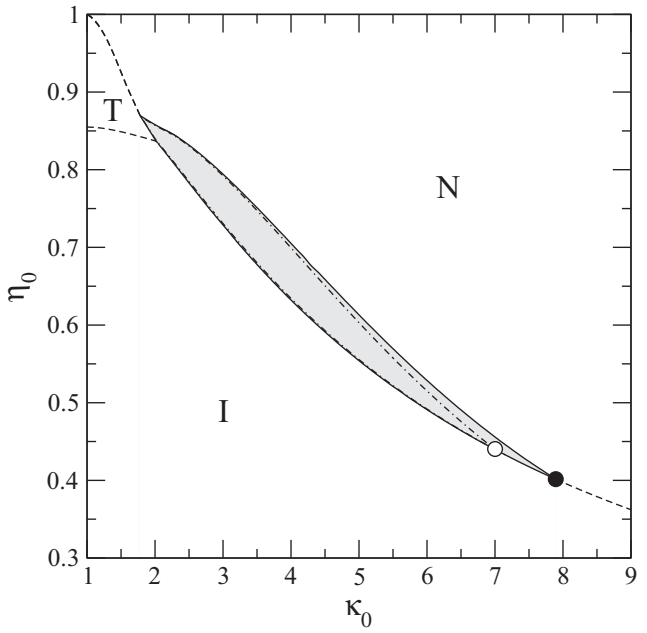

FIG. 5. Phase diagram for $\Delta_0 = 0.408$ and $q = 1$ (solid lines) and $\Delta_0 = 0.408$ and $q = 2$ (dot-dashed lines). Shown with closed and open circles are the I-N tricritical points corresponding to $q = 1$ and 2, respectively.

DF predicts a second-order I-N transition for most particle shapes, HRs being an important exception: The I-N and T-N transitions are of first order for aspect ratios between two (N-T and I-N) tricritical points. The broadening of the I-N coexisting region found here is related, in analogy to three dimensions, to a demixing like mechanism: The N and I phases are preferentially populated by long and small rods, respectively (the so-called fractionation effect). We can see from Fig. 4 that the T phase slightly destabilizes with polydispersity as we have already discussed in Sec. II D.

In Fig. 4(b) we show a close-up of the phase diagram around the left T-N tricritical point (closed circle). Note that the T_1-N_0 cloud binodal (the lower dot-dashed curve) ends up at an aspect ratio value κ_0 (lower square) slightly below that corresponding to the end of the T_0-N_1 binodal (upper square). This result suggests that the system could exhibit a triple I-T-N coexistence for aspect ratios located between the two vertical dotted lines.

The phase diagram corresponding to the selected parent distribution function with $q = 2$ (that with a Gaussian decay) is shown in Fig. 5 for the same $\Delta_0 = 0.408$. For comparison we show in the same figure the case $q = 1$. We observe that the cloud binodals corresponding to the I_1-N_0 coexistence for $q = 1$ and 2 coincide. On the other hand, the cloud binodal of the I_0-N_1 coexistence for $q = 2$ is located, in particular for large aspect ratios, below that of $q = 1$, reducing in this way the coexistence gap and consequently moving the I-N tricritical point from $\kappa_0^{(t)} \approx 7.9$ to $\kappa_0^{(t)} \approx 7.05$. We can conclude from this result that the position of the tricritical point depends not only of the first two moments of the parent distribution function (both are the same for $q = 1$ and 2), but also on higher moments, which are certainly different for the Schulz and Gaussian-like distributions. Through a bifurcation analysis of the free energy with respect to the Fourier components of an incipient N phase performed around the tricritical point, we can obtain an analytic equation relating the position of this point with these moments. This analysis was done for binary mixtures of HRs in Ref. [63]. The reduction of the coexistence gap with q reflects the lesser relevance of long rods on the phase behavior for distributions with strong decay.

B. Orientational ordering

In this section we discuss the orientational ordering of rectangles at equilibrium. To this purpose we first show the coexisting angular distribution functions $h^{(\alpha)}(\phi)$ as calculated from Eq. (28) corresponding to a stable I-N phase separation for $\kappa_0 = 3.2$, $q = 1$, and $\Delta_0 = 0.408$. The cloud and shadow N distributions are plotted in Fig. 6(a) with solid and dashed lines, respectively. The sharp peaks at 0 and π show the strong N ordering present in the fluid, while a rather small oscillation around $\pi/2$ indicates the closeness of the system to the region of T phase stability ($1 \leqslant \kappa_0 \lesssim 2$). Also, the cloud and shadow N distributions are very similar, with the latter

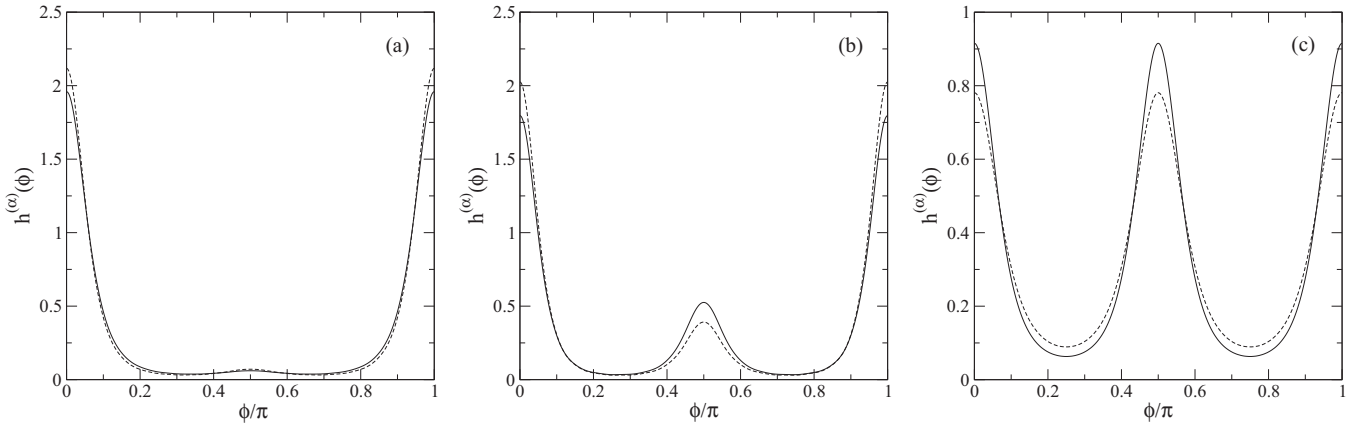

FIG. 6. Angular distribution functions $h^{(\alpha)}(\phi)$ for the $\alpha = (N,T)_1$ (solid lines) and $\alpha = (N,T)_0$ (dashed lines) phases corresponding to (a) the I-N coexistence for $\kappa_0 = 3.2$ and (b) and (c) the T-N coexistence for $\kappa_0 = 1.9$. We show (b) $h^{(N)}(\phi)$ and (c) $h^{(T)}(\phi)$. The values of q and Δ_0 were fixed to 1 and 0.4068, respectively.

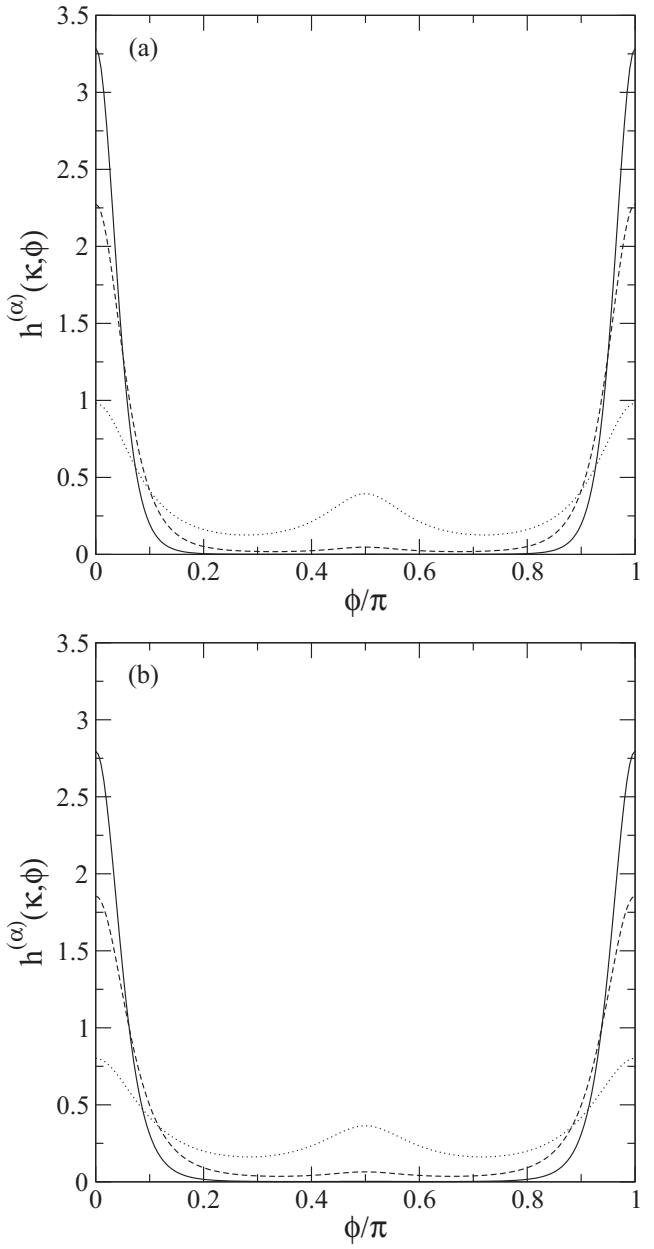

FIG. 7. Orientational distribution functions of rectangles of aspect ratios $\kappa = 1.5$ (dotted lines), 3 (dashed lines), and 5 (solid lines) corresponding to (a) the I_0-N_1 coexistence and (b) the I_1-N_0 coexistence of a polydisperse mixture with $q = 1$, $\kappa_0 = 3$, and $\Delta_0 = 0.408$.

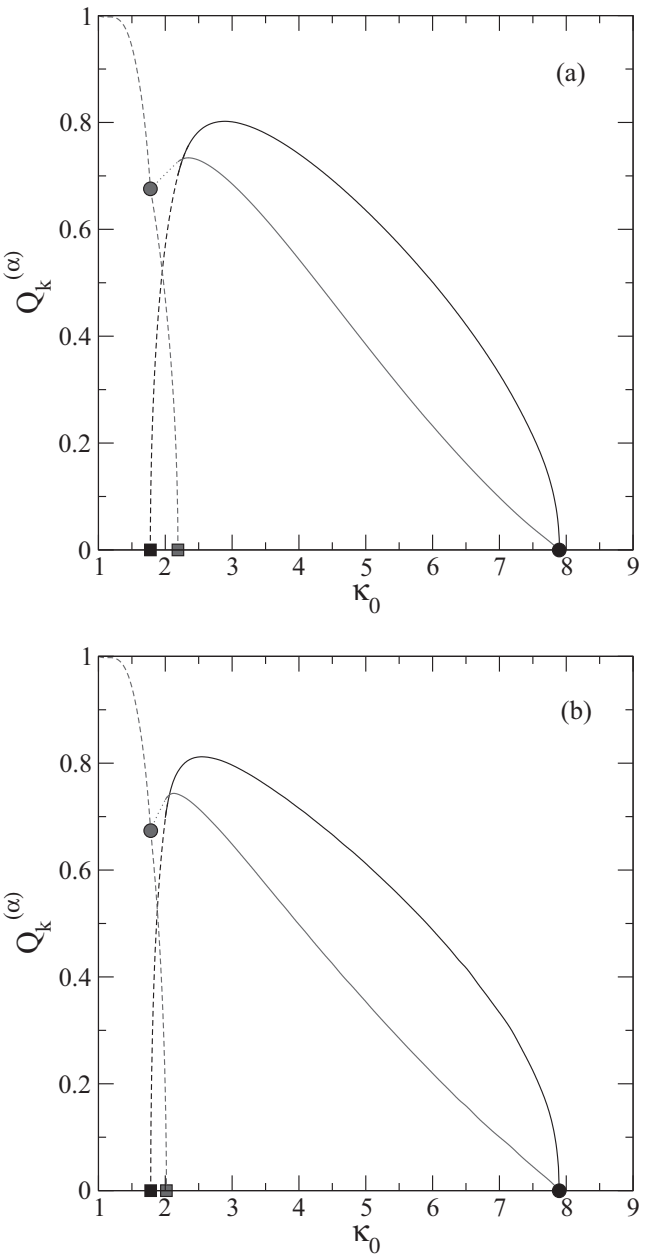

FIG. 8. Order parameters $Q_j^{(\alpha)}$ ($j = 1,2$, and $\alpha = N,T$) as a function of κ_0 for $\Delta_0 = 0.408$, $q = 1$, and (a) $\gamma_N = 1$ and (b) $\gamma_N = 0$. Different lines represent the order parameters along the I-N (solid lines) or T-N (dashed lines) coexistence. The order parameters $Q_1^{(\alpha)}$ and $Q_2^{(\alpha)}$ are shown in black and gray, respectively. Shown with gray and black closed circles are the left T-N and right I-N tricritical points, while the squares represent the values of κ_0 where $Q_2^{(\alpha)} = 0$.

showing a slightly higher ordering of particles. We show these distributions for the same values of q and Δ_0 but this time selecting $\kappa_0 = 1.9$ where the T-N coexistence is stable. The results are shown in Figs. 6(b) and 6(c) for the N and T phases, respectively. Now the N phase develops a well defined central peak at $\pi/2$ reflecting a high proportion of small rectangles with T-like ordering. Again the shadow N phase exhibits a slightly higher degree of N ordering and consequently a lesser proportion of small rectangles with T-like configurations. The coexisting T distributions [see Fig. 6(c)] have a periodicity of $\pi/2$ (the central peak is of the same height as those located at 0 and π) reflecting the T symmetry: The system is invariant under rotations of $\pi/2$. The cloud T phase has a higher degree of ordering than its shadow counterpart.

A better understanding of the degree of particle ordering at I-N coexistence can be reached through the calculation of the angular distribution function of species of a certain aspect ratio κ, $h^{(\alpha)}(\kappa,\phi)$, as defined by Eq. (27). It is expected that the N (T) ordering increases (decreases) with κ, an assertion well supported by the N distributions shown in Fig. 7 and calculated for the parameters $q = 1$, $\Delta_0 = 0.408$, $\kappa_0 = 3$, and

three different values of κ: 1.5 (dotted lines), 3 (dashed lines), and 5 (solid lines). The small species, being the less ordered, present a high proportion of T-like configurations, while the large ones exhibit a high degree of uniaxial N ordering. Again the cloud distributions [Fig. 7(a)] reflect a higher ordering than their shadow counterparts [Fig. 7(b)], a fact already pointed out before when we discussed the behavior of $h^{(\alpha)}(\phi)$ for $\kappa_0 = 3.2$.

The global ordering along the SOLs and binodal curves of the phase diagram, shown in Fig. 4, is calculated through the order parameters $Q_{1,2}^{(\alpha)}$ [see Eq. (30)]. These are plotted in Fig. 8 as functions of κ_0. For large values of κ_0 not close enough to the I-N tricritical point $\kappa_0^{t_2}$, the N order parameter $Q_1^{(N)}$ along the I-N coexistence is relatively high and always above the T order parameter $Q_2^{(N)}$. Obviously, at the I-N tricritical point they both become zero. As κ_0 decreases from $\kappa_0^{t_2}$ the T and N order parameters increase, both reaching their maxima at slightly different values close to $\kappa_0 = 3$. Just below $\kappa_0 = 3$ a crossover between $Q_1^{(N)}$ and $Q_2^{(N)}$ takes place. A slight decrease of κ_0 from this crossover gives $Q_2^{(N)} > Q_1^{(N)}$, a clear sign of the presence of a secondary peak at $\pi/2$ in the angular distribution function. Then the I-N transition is substituted by the T-N one and $Q_1^{(N)}$ decreases to zero at the T-N tricritical point $\kappa_0^{t_1}$. The order parameter $Q_2^{(N)}$ also decreases to a lesser extent up to the value shown with a gray circle (the T-N tricritical point). From this point $Q_2^{(T)}$ increases along the T-N SOL up to its maximum allowed value 1 as $\kappa_0 \to 1$, while it decreases along the T-N coexistence binodal as κ_0 is increased up to κ_0^c (shown with a gray square) where $Q_2^{(T)} = 0$. In Fig. 8(a) this point corresponds to the top black square shown in Fig. 4(b) where the cloud binodals of the T_0-N_1 (left from κ_0^c) and the I_0-N_1 (right from κ_0^c) coexistence meet. In a similar way in Fig. 8(b) the gray square indicates the crossing point between the cloud binodals of the T_1-N_0 and the I_1-N_0 coexistence and consequently $Q_2^{(T)}$ departs from zero along T_1-N_0 as κ_0 is decreased from κ_0^c. However, now this value coincides with that of the critical end point [bottom black square in Fig. 4(b)] where the I-T SOL ends.

The difference $\Delta\kappa \equiv \kappa_0^c - \kappa_0^{t_1}$ between the aspect ratios corresponding to those of the tricritical and critical end points [see the squares in Figs. 8(a) and 8(b)] depends on which of the phases is considered to be the cloud one. When $\gamma_N = 1$ [Fig. 8(a)], i.e., for the $(I,T)_0$-N_1 coexistence, this difference is

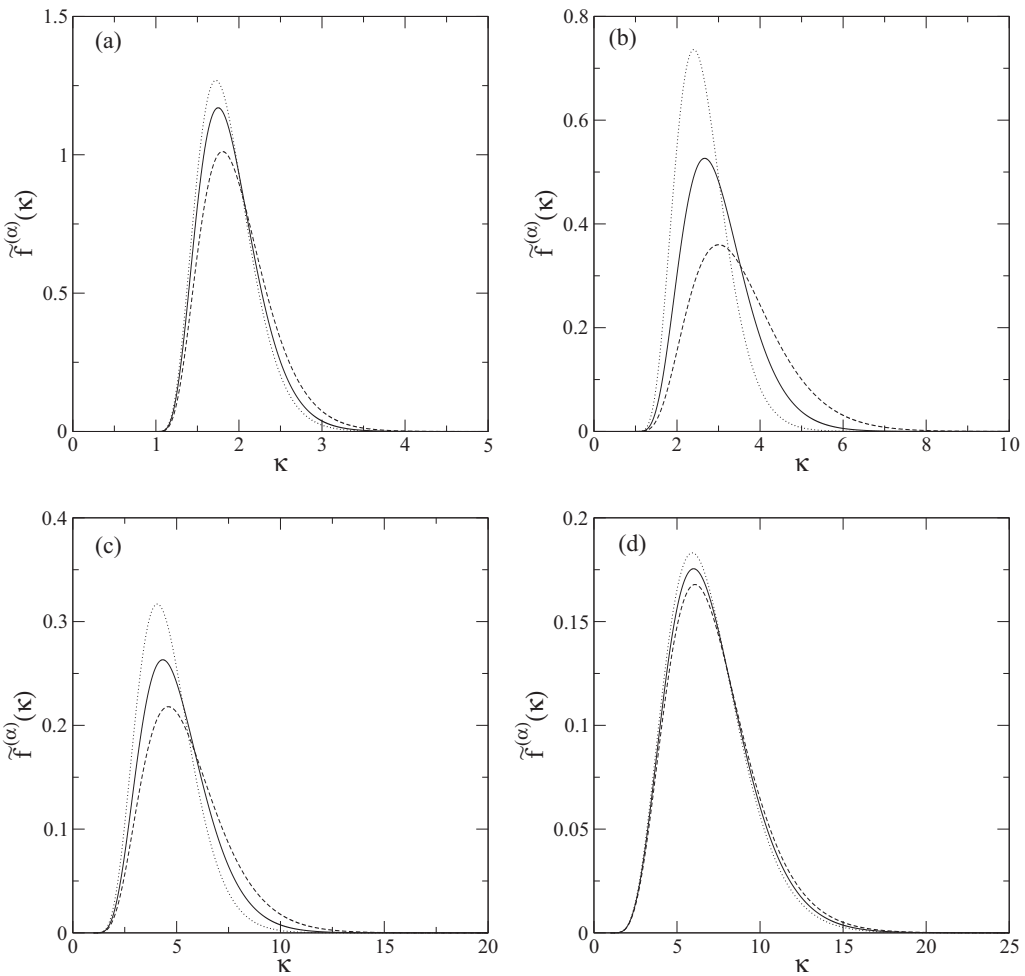

FIG. 9. Distribution functions $\tilde{f}^{(\alpha)}(\kappa)$ of the (a) T-N and (b)–(d) I-N coexisting phases for (a) $\kappa_0 = 1.9$, (b) $\kappa_0 = 3$, (c) $\kappa_0 = 5$, and (d) $\kappa_0 = 7$. The parent distribution function $f_0(\kappa)$ (coinciding with the distributions of the cloud coexisting phases) was selected to be of Schultz type ($q = 1$) with a polydisperse coefficient $\Delta_0 = 0.408$ and is plotted with solid lines. The distributions corresponding to (a)–(d) N_0 are plotted with dashed lines, while those of (a) T_0 and (b)–(d) I_0 are plotted with dotted lines.

clearly larger than that corresponding to $\gamma_N = 0$, the $(I,T)_1$-N_0 coexistence [Fig. 8(b)]. This behavior is related to the already discussed fact about the possible existence of a triple I-N-T coexistence [see Fig. 4(b)] for values of mean aspect ratios located between these points.

C. Fractionation as a function of κ_0

This section is devoted to exploring in detail the fractionation of different species between the coexisting phases. To this purpose we have fixed the values of the mean aspect ratio κ_0 to one of the values of the set $\{3,5,7\}$. Also we have selected the polydisperse coefficient of the Schulz-type ($q = 1$) distribution function to be $\Delta_0 = 0.408$ as before. Further, we numerically solved Eqs. (14) and (20) for chemical and mechanical equilibrium between cloud-shadow coexisting phases. As a result we found the normalized length distributions $\tilde{f}^{(\alpha)}(\kappa)$ obtained from (32)–(34) for the shadow I, T, or N phases. We should bear in mind that the cloud phases always follow the distribution $f_0(\kappa)$. All these distributions are plotted in Fig. 9. We can appreciate a clear fractionation of small and long species between cloud-shadow phases. The small ones preferentially populate the I or T phases, while the N phase is rich in long species: See how the maxima of the I and T distributions are clearly located left of those of the N distributions. Also the latter has a slower decay, indicating a higher fraction of long species. As we can see from the figure, the fractionation is much more dramatic for $\kappa_0 = 3$, which is clearly correlated with the value at which the N phase has the highest order parameter $Q_1^{(N)}$ (see Fig. 8). As we move away from this value in the directions of both tricritical points $\kappa_0^{t_i}$ the system exhibits fractionation but to a lesser extent due to the weaker character of the (I,T)-N phase transition.

Another important consequence of the fractionation is related to the values of the dimensionless moments of the distribution functions $\eta_0^{(i,\alpha)}$ at coexistence. In Fig. 10 we plot these moments as a function of γ_I for $q = 1$, $\kappa_0 = 3$, and $\Delta_0 = 0.408$. The inequalities $\eta_0^{(0,I)} > \eta_0^{(0,N)}$ and $\eta_0^{(1,N)} > \eta_0^{(1,I)}$ are always fulfilled, which constitutes a direct consequence of how different the shapes of $\tilde{f}^{(I)}(\kappa)$ and $\tilde{f}^{(N)}(\kappa)$ are, as discussed previously. Integrating the sharpest strongly decayed function $\kappa^i\,\tilde{f}^{(I)}(\kappa)$ over κ for $i = 0$ ($i = 1$) gives us a value of $\eta_0^{(0,I)}$ ($\eta_0^{(1,I)}$) greater (less) than that obtained from the integration of the slower decaying function $\kappa^i\,\tilde{f}^{(N)}(\kappa)$.

To finish this section we present in Fig. 11 how $\langle\kappa\rangle_{\tilde{f}^{(\alpha)}(\kappa)}$ [the average aspect ratio with respect to the coexisting shadow distribution $\tilde{f}^{(\alpha)}(\kappa)$] evolves as a function of κ_0 for $\Delta_0 = 0.408$. As expected, this average, which directly measures the fractionation, becomes equal to κ_0 at both tricritical points (closed circles), while it reaches its maximum (minimum) value at $\kappa_0 \sim 3$ when averaged with respect to N_0 (I_0) distributions. This qualitative behavior is similar for both the Schulz ($q = 1$) and Gaussian-tailed ($q = 2$) distributions. However, the latter provokes less fractionation.

D. Fractionation as a function of Δ_0

To finish the discussion on fractionation we present in Fig. 12 the results regarding the behavior of the dimensionless zeroth moments $\eta_0^{(0,\alpha)}$ of coexisting cloud and shadow phases

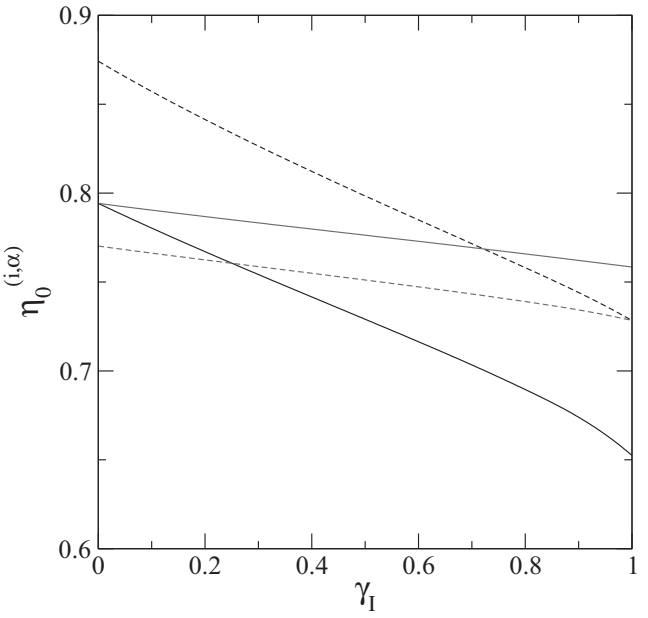

FIG. 10. Moments $\eta_0^{(0,\alpha)}$ (black lines) and $\eta_0^{(1,\alpha)}$ (gray lines) of the I (dashed lines) and N (solid lines) coexisting distribution functions as a function of the fraction of volume occupied by the I phase γ_I for $\kappa_0 = 3$, $q = 1$, and $\Delta_0 = 0.408$.

as a function of polydispersity for fixed $\kappa_0 = 3$ [Fig. 12(a)] and $\kappa_0 = 7$ [Fig. 12(b)] and selecting $f_0(\kappa)$ to be of Schulz type ($q = 1$). We observe a dramatic widening of the coexistence region, i.e., the gap between the moments corresponding to I_1 and N_1 phases (solid lines) greatly increases with Δ_0 (for $\kappa_0 = 7$ the same occurs but beyond the tricritical point). Also, for $\kappa_0 = 3$ and zero polydispersity the moments of the shadow

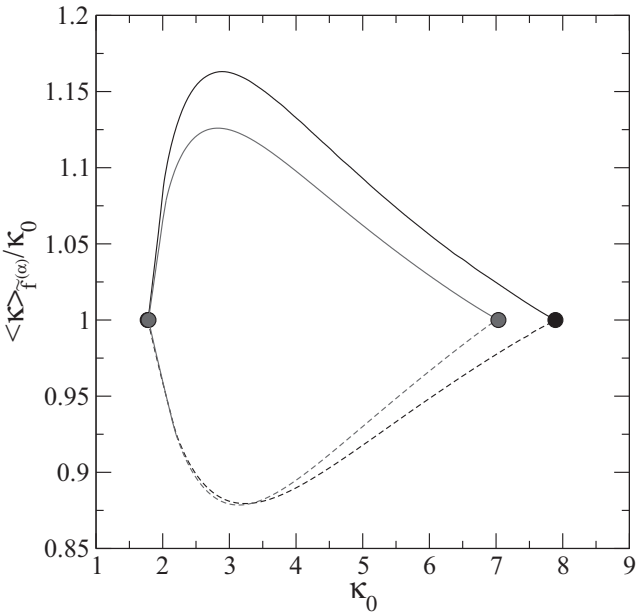

FIG. 11. Averaged over $\tilde{f}^{(\alpha)}(\kappa)$ aspect ratio $\langle\kappa\rangle_{\tilde{f}^{(\alpha)}}$ in units of the mean aspect ratio κ_0 along the coexisting $(I,T)_0$ (dashed lines) and N_0 (solid lines) binodals for $q = 1$ (black lines) and $q = 2$ (gray lines). The polydispersity is fixed to $\Delta_0 = 0.408$.

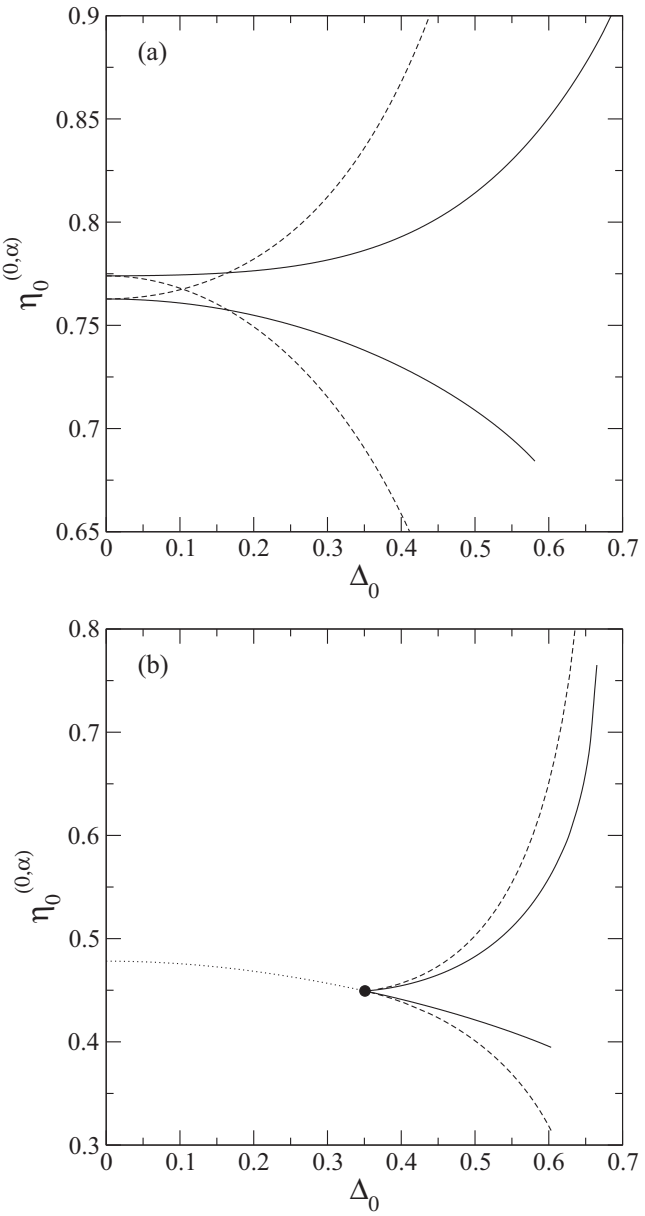

FIG. 12. Zeroth moments $\eta_0^{(0,\alpha)}$ ($\alpha = I, N$) as a function of Δ_0 for $q = 1$ and (a) $\kappa_0 = 3$ and (b) $\kappa_0 = 7$. Shown with solid lines are the values of $\eta_0^{(0,\alpha)}$ for the I_1 and N_1 coexisting (with N_0 and I_0) phases, respectively. The $(I,N)_0$ coexisting curves are shown with dashed lines. The black circle in (b) shows the position of the tricritical point, while the dotted line represents the I-N SOL.

I and N phases (dashed lines) obviously coincide with those of the cloud phases and they compare as usual: $\eta_0^{(0,I)} < \eta_0^{(0,N)}$. However, as Δ_0 increases they exhibits a crossover at $\Delta_0 \approx 0.1$ and the former relation is inverted: $\eta_0^{(0,I)} > \eta_0^{(0,N)}$. This in turns means that the I shadow distribution function $f^{(I)}(\kappa)$ (which is not normalized) exhibits, as a result of strong fractionation, a sharper peak located at relatively small values of κ. On the other hand, the N shadow distribution $f^{(N)}(\kappa)$ shows a more smeared peak located at larger values of κ (see Fig. 9). These differences in the shapes of distributions result in $\int d\kappa\, f^{(I)}(\kappa) > \int d\kappa\, f^{(N)}(\kappa)$. Interestingly, this crossover does not exist for $\kappa_0 = 7$: At the tricritical point the moments

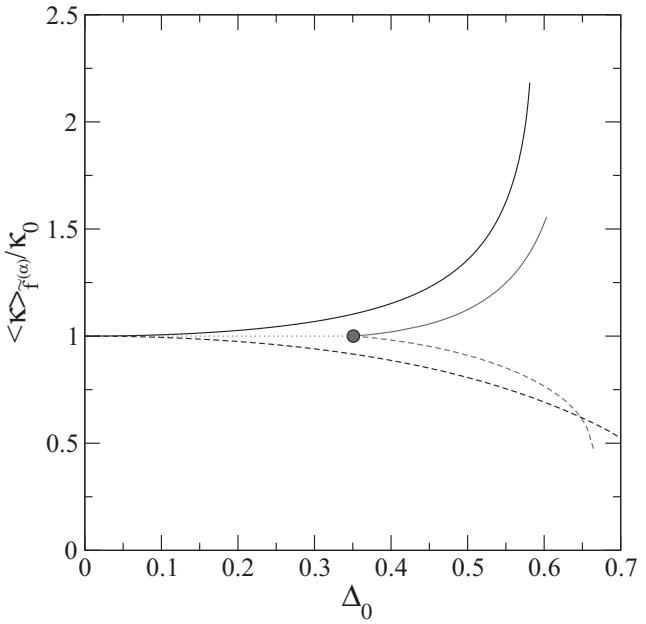

FIG. 13. Averaged over $\tilde{f}^{(\alpha)}(\kappa)$ [$\alpha = I$ (dashed lines) and $\alpha = N$ (solid lines)] aspect ratio $\langle\kappa\rangle_{\tilde{f}^{(\alpha)}}$ in units of κ_0 as a function of Δ_0 for $\kappa_0 = 3$ (black lines) and $\kappa_0 = 7$ (gray lines) and $q = 1$.

are equal, while beyond it the fractionation mechanism always gives $\eta_0^{(0,I)} > \eta_0^{(0,N)}$. A more clear measure of fractionation, given by $\langle\kappa\rangle_{\tilde{f}^{\alpha}}$, is plotted as a function of Δ_0 along the same shadow curves in Fig. 13. For $\kappa_0 = 3$ ($\kappa_0 = 7$) the aspect ratio, averaged with respect to the shadow N (I) distribution, can reach values as large (low) as $2\kappa_0$ ($\kappa_0/2$) for high enough Δ_0, a clear sign of the presence of strong fractionation.

E. Tricritical points

The last study we have carried out concerns the location of the I-N tricritical point as a function of polydispersity. To this purpose we fixed the value of κ_0 and calculated the I_0-N_1 coexistence for high enough values of Δ_0 [selected in such a way as to guarantee a first-order I-N transition and thus to find a nontrivial numerical solution of Eq. (14)]. Then we gradually decreased the value of Δ_0 and used as new initial guesses those found in the previously converged iterations. This process is repeated up to that value of Δ_0 for which the order parameter $Q_1^{(N)}$ is negligibly small. Finally, an accurate extrapolation (using a cubic-spline fitting) of $Q_1^{(N)}$ to zero gives us the value Δ_0^* at which the first-order transition becomes of second order, i.e., the position of the tricritical point. This process was carried out for a set of aspect ratios and the results are shown in Fig. 14. The open circles show our selected values of κ_0 and the curve is an Akima spline fitting to guide the eyes. This curve has certain credibility only as an interpolation fitting. However, we have decided to use the same fitting to conjecture the value of Δ_0^* in the limit $\kappa_0 \to \infty$. This result might indicate that there exists a terminal polydispersity, around the value of 0.7, beyond which the I-N transition becomes of first order for any κ_0. We may certainly solve this conjecture by performing a bifurcation analysis around the tricritical point in such a way as to find an analytic expression for Δ_0^* as a

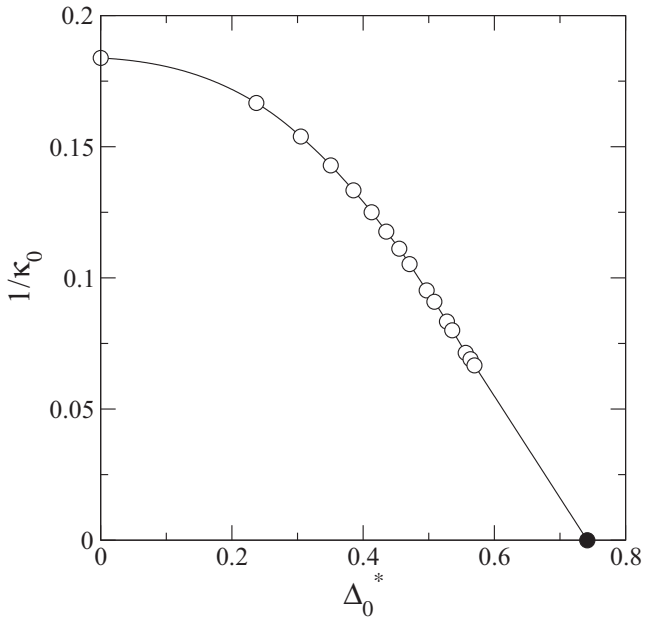

FIG. 14. Plot of κ_0^{-1} as a function of Δ_0^* (the I-N tricritical point value) for $q = 1$. The open circles correspond to the calculated values, while the solid curve is an Akima cubic-spline fitting. The black circle indicates the extrapolated value of Δ_0^* when $\kappa_0 \to \infty$.

function not only of κ_0 but also of higher moments of the distribution $f_0(\kappa_0)$. This study, as well as its generalization for any particle shape (polydisperse hard discorectangles, hard ellipses, etc.), is beyond the scope of the present paper; however, it should be able to shed some light on the character (second vs first) of the I-N transition that mean-field theories predict for different polydisperse particle shapes.

IV. CONCLUSION

We have extended the SPT of HR fluid from its multicomponent version to consider a continuous length polydispersity. Using this formalism, we derived simplified coexistence equations by using the Fourier expansions of the angular moment profiles. The numerical solution of the obtained set of equations for the Fourier components and for different values of the mean aspect ratio and polydispersity allowed us to obtain the phase diagram of the system. We have not taken any functional ansatz to parametrize the density profile. Thus our calculations are exact up to the errors associated with the truncation of the Fourier series. The main results can be summarized as follows. (i) The I-N transition becomes stronger with polydispersity, i.e., the coexistence gap becomes wider and the tricritical point moves to higher values of κ_0. (ii) The stability of the T phase slightly decreases with Δ_0. (iii) There exists strong fractionation between the coexisting phases that becomes stronger at $\kappa_0 \sim 3$ and decreases as we approximate the T-N or I-N tricritical points. The fractionation for a Schulz-type parent distribution function is stronger than that obtained for a Gaussian-tailed distribution. As usual, the N phase is rich in long particles, while the I or T phases are highly populated by the smaller particles. (iv) The orientational ordering of coexisting species of different κ is in general different: The small species, those with $\kappa \gtrsim 1$, have a low orientational ordering and tend to align in T-like configurations, while long species contribute to stabilize the uniaxial N. This effect is more pronounced for $\kappa_0 \sim 3$. (v) The locations of tricritical points are severely affected by polydispersity and our results might suggest the existence of a terminal polydispersity beyond which the I-N transition becomes of first order. We require further calculations to definitively settle this point.

A recent experiment on magnetic polydisperse nanorods that are strongly confined between lamellar layers (an experimental realization of a quasi-2D hard-rod fluid) shows a first-order I-N transition with the N director being parallel to the plane of the layers [37]. As we have shown in the present work, when the polydispersity is high enough the character of the I-N transition could change from second to first order. Thus the polydispersity could explain the experimental results obtained in Ref. [37].

Recently, a T phase was found as a stationary state in vertically vibrated monolayers of granular cylinders [62]. If we take into account the strong tendency of cylinders to form clusters of approximately rectangular shape then the system could be viewed as a polydisperse mixture of HRs. The mean value κ_0 of the aspect ratio of this polydisperse mixture from which the T phase was found is always below 2.21, a value very similar to that predicted by the SPT.

We have not considered the presence of nonuniform phases (like smectic or crystal) in the present study. For low polydispersity they become stable at high densities. However, when polydispersity increases they rapidly destabilize, so the results shown here, especially those obtained for high enough Δ_0, could be qualitatively confirmed by experimental realizations of a 2D hard-rectangle fluid. One of them could be mechanically vibrated monolayers of granular cylinders. Recent experiments on such systems have confirmed the presence of strong T, N [38,41], and smectic [62] ordering of rods, which strongly depends on the aspect ratio and packing fraction. It would be interesting to study the effect of length polydispersity on the stability of the liquid-crystal textures found in Ref. [62].

ACKNOWLEDGMENT

Financial support from MINECO (Spain) under Grant No. FIS2015-66523-P is acknowledged.

APPENDIX: THE I_1-N_0 COEXISTENCE EQUATIONS

For $q = 1$ and $\gamma_I = 1$ the integral with respect to κ in the set of equations (14) corresponding to the I-N coexistence calculations can be performed analytically, resulting in the following set of equations for the variables $\eta_j^{(i,N)}$:

$$\eta_j^{(i,N)} = \kappa_0^{-1}\eta_j^{(0,N)}\delta_{i1} + D_{j0}\eta_0\left(1-\kappa_0^{-1}\right)^i \int_0^1 du\,\cos(\pi j u)\frac{e^{-R_0(\pi u)}}{[1+R_1(\pi u)]^{\nu+i+1}}, \tag{A1}$$

where we have defined the functions

$$R_0(\phi) = \ln\left(\frac{1-\eta_0}{1-\eta_0^{(1,N)}}\right) + \frac{4}{\pi}\left[\frac{\eta_0^{(1,N)} + \eta_0^{(0,N)}\kappa_0^{-1} - \sum_{j\geqslant 1} s_{2j}^{(N)} g_{2j}\cos(2j\phi)}{1-\eta_0^{(1,N)}} - \frac{\eta_0}{1-\eta_0}\left(1+\kappa_0^{-1}\right)\right], \tag{A2}$$

$$R_1(\phi) = \frac{2(\kappa_0-1)}{\pi(\nu+1)}\left[\frac{\eta_0^{(1,N)} + \eta_0^{(0,N)}\kappa_0^{-1} - \sum_{j\geqslant 1} s_{j}^{(N)} g_{j}\cos(j\phi)}{1-\eta_0^{(1,N)}} - \frac{\eta_0}{1-\eta_0}\left(1+\kappa_0^{-1}\right)\right], \tag{A3}$$

with $s_j^{(N)} \equiv \eta_j^{(1,N)} + (-1)^j \kappa_0^{-1}\eta_j^{(0,N)}$ and $g_j \equiv (4j^2-1)^{-1}$. For the cloud I coexisting phase we have $\eta_0^{(i,I)} = \eta_0$. For $q = 2$ and $\gamma_I = 1$ we obtain

$$\eta_j^{(i,N)} = \kappa_0^{-1}\eta_j^{(0,N)}\delta_{i1} + \eta_0\left(1-\kappa_0^{-1}\right)^i \frac{\Gamma(\nu+i+1)}{2^{(\nu+i-1)/2}\Gamma[(\nu+i+1)/2]}\int_0^1 du\,\cos(\pi j u) e^{-R_0(\pi u)} e^{\mathcal{R}_1^2(\pi u)/8} D_{-(\nu+i+1)}[\mathcal{R}_1(\pi u)/\sqrt{2}], \tag{A4}$$

where the function $R_0(\phi)$ is the same as (A2), while

$$\mathcal{R}_1(\phi) = R_1(\phi)\frac{(\nu+1)\Gamma[(\nu+1)/2]}{\Gamma[(\nu+2)/2]}. \tag{A5}$$

Here $D_\mu(x)$ is the parabolic cylinder function. We used a FORTRAN subroutine provided in Ref. [65] to numerically evaluate $D_\mu(x)$.

[1] F. M. van der Kooij, K. Kassapidou, and H. N. W. Lekkerkerker, Nature (London) **406**, 868 (2000).
[2] F. M. van der Kooij, D. van der Beek, and H. N. W. Lekkerkerker, J. Phys. Chem. B **105**, 1696 (2001).
[3] A. V. Petukhov, D. van der Beek, R. P. A. Dullens, I. P. Dolbnya, G. J. Vroege, and H. N. W. Lekkerkerker, Phys. Rev. Lett. **95**, 077801 (2005).
[4] P. Woolston and J. S. van Duijneveldt, J. Chem. Phys. **142**, 184901 (2005).
[5] G. J. Vroege, D. M. E. Thies-Weesie, A. V. Petukhov, B. J. Lemaire, and P. Davidson, Adv. Mater. **18**, 2565 (2006).
[6] E. van den Pol, D. M. E. Thies-Weesie, A. V. Petukhov, G. J. Vroege, and K. Kvashnina, J. Chem. Phys. **129**, 164715 (2008).
[7] A. A. Verhoeff, H. H. Wensink, M. Vis, G. Jackson, and H. N. W. Lekkerkerker, J. Phys. Chem. B **113**, 13476 (2009).
[8] D. Sun, H.-J. Sue, Z. Cheng, Y. Martínez-Ratón, and E. Velasco, Phys. Rev. E **80**, 041704 (2009).
[9] D. V. Byelov, M. C. D. Mourad, I. Snigireva, A. Snigirev, A. V. Petukhov, and H. N. W. Lekkerkerker, Langmuir **26**, 6898 (2010).
[10] A. B. G. M. Leferink op Reinink, E. van den Pol, D. V. Byelov, A. V. Petukhov, and G. J. Vroege, J. Phys.: Condens. Matter **24**, 464127 (2012).
[11] N. Clarke, J. A. Cuesta, R. Sear, P. Sollich, and A. Speranza, J. Chem. Phys. **113**, 5817 (2000).
[12] P. Sollich, J. Phys.: Condens. Matter **14**, R79 (2002).
[13] A. Speranza and P. Sollich, J. Chem. Phys. **117**, 5421 (2002).
[14] A. Speranza and P. Sollich, Phys. Rev. E **67**, 061702 (2003).
[15] S. Fraden, G. Maret, and D. L. D. Caspar, Phys. Rev. E **48**, 2816 (1993).
[16] D.-H. Nguyen, E. Azéma, F. Radjai, and P. Sornay, Phys. Rev. E **90**, 012202 (2014).
[17] J. Viamontes, P. W. Oakes, and J. X. Tang, Phys. Rev. Lett. **97**, 118103 (2006).
[18] T. J. Scluckin, Liq. Cryst. **6**, 111 (1989).
[19] M. A. Bates and D. Frenkel, J. Chem. Phys. **109**, 6193 (1998).
[20] M. A. Bates and D. Frenkel, J. Chem. Phys. **110**, 6553 (1999).
[21] Y. Martínez-Ratón and J. A. Cuesta, Phys. Rev. Lett. **89**, 185701 (2002).
[22] Y. Martínez-Ratón and J. A. Cuesta, J. Chem. Phys. **118**, 10164 (2003).
[23] H. H. Wensink and G. J. Vroege, J. Chem. Phys. **119**, 6868 (2003).
[24] A. Speranza and P. Sollich, J. Chem. Phys. **118**, 5213 (2003).
[25] A. Richter and T. Gruhn, J. Chem. Phys. **125**, 064908 (2006).
[26] M. J. Green, A. N. G. Parra-Vasquez, N. Behabtu, and M. Pasquali, J. Chem. Phys. **131**, 084901 (2009).
[27] E. van den Pol, A. Lupascu, M. A. Diaconeasa, A. V. Petukhov, D. V. Byelov, and G. J. Vroege, J. Phys. Chem. Lett. **1**, 2174 (2010).
[28] Y. Martínez-Ratón and E. Velasco, J. Chem. Phys. **134**, 124904 (2011).
[29] M. J. Green, J. Polym. Sci. B **50**, 1321 (2012).
[30] Y. Martínez-Ratón and E. Velasco, J. Chem. Phys. **137**, 134906 (2012).
[31] E. Velasco and Y. Martínez-Ratón, Phys. Chem. Chem. Phys. **16**, 765 (2014).
[32] U. Agarwal and F. A. Escobedo, J. Chem. Phys. **137**, 024905 (2012).
[33] D. Ioffe, Y. Velenik, and M. Zahradnik, J. Stat. Phys. **122**, 761 (2006).
[34] J. M. Tavares, B. Holder, and M. M. Telo da Gama, Phys. Rev. E **79**, 021505 (2009).
[35] L. G. López, D. H. Linares, and A. J. Ramirez-Pastor, Phys. Rev. E **80**, 040105(R) (2009).
[36] N. G. Almarza, J. M. Tavares, and M. M. Telo da Gama, Phys. Rev. E **82**, 061117 (2010).
[37] K. Slyusarenko, D. Constantin, and P. Davidson, J. Chem. Phys. **140**, 104904 (2014).
[38] V. Narayan, N. Menon, and S. Ramaswamy, J. Stat. Mech. (2006) P01005.

[39] J. Galanis, D. Harries, D. L. Sackett, W. Losert, and R. Nossal, Phys. Rev. Lett. **96**, 028002 (2006).
[40] J. Galanis, R. Nossal, W. Losert, and D. Harries, Phys. Rev. Lett. **105**, 168001 (2010).
[41] T. Müller, D. de las Heras, I. Rehberg, and K. Huang, Phys. Rev. E **91**, 062207 (2015).
[42] J. M. Kosterlitz and D. J. Thouless, J. Phys. C **6**, 1181 (1973).
[43] M. A. Bates and D. Frenkel, J. Chem. Phys. **112**, 10034 (2000).
[44] M. C. Lagomarsino, M. Dogterom, and M. Dijkstra, J. Chem. Phys. **119**, 3535 (2003).
[45] A. C. D. van Enter and S. B. Shlosman, Phys. Rev. Lett. **89**, 285702 (2002).
[46] R. L. C. Vink, Phys. Rev. Lett. **98**, 217801 (2007).
[47] L. G. López, D. H. Linares, A. J. Ramirez-Pastor, and S. A. Cannas, J. Chem. Phys. **133**, 134706 (2010).
[48] J. A. Cuesta, C. F. Tejero, and M. Baus, Phys. Rev. A **39**, 6498 (1989).
[49] J. A. Cuesta and D. Frenkel, Phys. Rev. A **42**, 2126 (1990).
[50] W. S. Xu, Y. W. Li, Z. Y. Sun, and L. J. An, J. Chem. Phys. **139**, 024501 (2013).
[51] G. Bautista-Carbajal and G. Odriozola, J. Chem. Phys. **140**, 204502 (2014).
[52] H. Schlacken, H. J. Mogel, and P. Schiller, Mol. Phys. **93**, 777 (1998).
[53] K. W. Wojciechowski and D. Frenkel, Comput. Methods Sci. Technol. **10**, 235 (2004).
[54] Y. Martínez-Ratón, E. Velasco, and L. Mederos, J. Chem. Phys. **122**, 064903 (2005).
[55] A. Donev, J. Burton, F. H. Stillinger, and S. Torquato Phys. Rev. B **73**, 054109 (2006).
[56] Y. Martínez-Ratón, E. Velasco, and L. Mederos, J. Chem. Phys. **125**, 014501 (2006).
[57] D. A. Triplett and K. A. Fichthorn, Phys. Rev. E **77**, 011707 (2008).
[58] K. Zhao, C. Harrison, D. Huse, W. B. Russel, and P. M. Chaikin, Phys. Rev. E **76**, 040401 (2007).
[59] K. Zhao, R. Bruinsma, and T. G. Masona, Proc. Natl. Acad. Sci. USA **108**, 2684 (2011).
[60] C. Avendaño and F. A. Escobedo, Soft Matter **8**, 4675 (2012).
[61] L. Walsh and N. Menon, J. Stat. Mech. (2016) 083302.
[62] M. González-Pinto, F. Borondo, Y. Martínez-Ratón, and E. Velasco, Soft Matter **13**, 2553 (2017).
[63] Y. Martínez-Ratón, E. Velasco, and L. Mederos, Phys. Rev. E **72**, 031703 (2005).
[64] D. de las Heras, Y. Martínez-Ratón, and E. Velasco, Phys. Rev. E **76**, 031704 (2007).
[65] S. Zhang and J. Jin, *Computation of Special Functions* (Wiley, New York, 1996).